Quantum phase diagrams for bosons in hexagonal optical potentials: A continuous-space quantum Monte Carlo study

Danilo Nascimento Guimaraes[1] and Laurent Sanchez-Palencia[1]

[1] *CPHT, CNRS, École Polytechnique, Institut Polytechnique de Paris, Palaiseau, France*

(Dated: May 7, 2026)

Hexagonal optical lattices, emulating graphene and hexagonal boron nitride (h-BN) structures, provide a versatile platform for exploring strongly correlated quantum matter. Using continuous-space exact diagonalization and quantum Monte Carlo simulations, we investigate the phase diagrams of ultracold bosons in honeycomb and h-BN lattices. For the honeycomb lattice, we find significant deviations from the standard Bose-Hubbard model even for strong lattice amplitudes. We observe suppressed Mott insulator lobes and the absence of higher-order insulating phases, attributed to strong density-assisted tunneling effects. In the h-BN case, a rich phase diagram emerges, featuring multiple Mott lobes with various sublattice occupations, driven by the interplay of lattice asymmetry, interactions, and particle filling. Our results highlight the necessity of continuous-space treatments for capturing the full complexity of bosonic quantum phases in hexagonal geometries, paving the way for experimental realizations with ultracold atoms and further theoretical work.

I. INTRODUCTION

Solid-state materials exhibit a remarkable diversity of geometric structures, arising from the interplay of atomic electronic configurations and complex interactions. Beyond conventional cubic lattices, these include triangular, checkerboard, and honeycomb lattices, as well as quasicrystals, and multilayer systems [1–5]. Such structures give rise to a wealth of nontrivial phenomena ranging from exotic superconductivity and anomalous quantum Hall effects to fractal behavior, localization, and topological phases, which are currently attracting considerable attention [6–12]. The challenge lies in unraveling the intricate interplay of matter-wave interference, electronic interactions, and geometric effects that underpin these phenomena. In parallel, ultracold atomic systems have emerged as a versatile platform for quantum simulation, offering unprecedented control over interaction strengths, sign, and range, as well as, lattice geometries and dynamical parameters [13–20]. By engineering laser configurations, exotic lattice structure, such as triangular, honeycomb, Lieb, and Kagome lattices, as well as superlattices and quasiperiodic lattices, can be emulated [21–35]. These systems allows us to not only revisit the physics of strongly correlated electronic systems but also explore new physics of bosonic quantum matter in such structures. Moreover, recent advances, including multi-frequency lattices and dynamical phase control, further expand the range of accessible geometries [36–39].

Hexagonal lattices, exemplified by graphene and certain carbon nanotubes [3, 40], are of particular interest due to their unique band structures, which feature Dirac cones, flat bands, and exaggerated correlation effects, as well as their rich topological properties [3, 41–43]. Up to date only a few experiments have realized hexagonal lattices but they have already facilitated studies of exotic effects, including multi-orbital superconductivity [44], antiferromagnetic Néel ordering [45], and Dirac point physics [26]. It is also worth mentioning cavity polariton systems with nanopillars arrays arranged in honeycomb geometry [46, 47]. Theoretically, tight-binding models have been extensively employed to describe the single-particle band structure of honeycomb and gapped-honeycomb systems [3, 48–50], while Bose–Hubbard models have been used to study superfluid–Mott transitions and superlattice-induced insulating phases [51–53]. Beyond, dynamical control of optical lattices has enabled the realization of hexagonal boron nitride (h-BN, aka gapped graphene) models [36], with recent theoretical work revealing transitions between Mott insulating, checkerboard and superfluid phases at unit filling, tunable by the lattice gap [53].

In this work, we investigate the dynamics of ultracold bosons in hexagonal optical potentials, including honeycomb and h-BN lattices. Using continuous-space calculations, we determine the band structure of these models, establishing the validity limits of tight-binding approximations and extracting their parameters. Moreover, quantum Monte Carlo (QMC) simulations yield exact phase diagrams at vanishingly small temperatures and arbitrary fillings. For the honeycomb lattice, we find standard superfluid and Mott insulator phases. However, we observe significant deviations from Bose-Hubbard models, even at strong lattice amplitudes where band structures are very well reproduced. For instance, for a lattice depth $V_0 = 15\,E_\mathrm{r}$, the lowest band is reproduced by the simplest tight-binding model with an accuracy of about 1% but the Bose–Hubbard approximation fails to describe but the first Mott lobe. These deviations are attributed to strong density-assisted tunneling effects beyond the Bose-Hubbard framework. For the h-BN lattice, our results unveil a rich phase diagram characterized by multiple Mott lobes with various fillings, hence extending the findings of Ref. [53] and highlighting the interplay of interactions, filling, and lattice geometry. Our work paves the way for experiments with ultracold atoms in hexagonal optical lattices and motivates further exploration of multilayer systems.

II. MODEL

The dynamics of a 2D gas of identical spinless bosons with mass m and repulsive two-body interactions is governed by the Hamiltonian

$$\hat{H} = \int d\mathbf{r}\, \hat{\Psi}^\dagger \left[\hat{H}_0 + \frac{1}{2} \int d\mathbf{r}'\, \hat{\Psi}'^\dagger U(\mathbf{r}-\mathbf{r}') \hat{\Psi}' \right] \hat{\Psi}, \quad (1)$$

where $\hat{\Psi}$ and $\hat{\Psi}'$ are, respectively, the field operators at positions $\mathbf{r}$ and $\mathbf{r}'$, $\hat{H}_0 = -\hbar^2\nabla^2/2m + V(\mathbf{r})$ is the one-body Hamiltonian with potential $V(\mathbf{r})$, and $U(\mathbf{r}-\mathbf{r}')$ is the two-body interaction potential. We consider the honeycomb-like lattice potential

$$V(\mathbf{r}) = 2V_0 \sum_{j=1}^{3} \cos(\mathbf{G}_j \cdot \mathbf{r} + \phi_j)\,, \quad (2)$$

where V_0 is the potential amplitude, the ϕ_j's are phases, and the $\mathbf{G}_j$'s are vectors with size π/a and arranged to form angles of $2\pi/3$ with each other. A possible implementation of such a potential with controlled parameters involves using multifrequency settings with three pairs of lasers [36], see Fig. 1(a). We then have $\mathbf{G}_j = \mathbf{k}_j - \mathbf{k}'_j$, where $\mathbf{k}_j$ and $\mathbf{k}'_j$ are the laser wavevectors with $|\mathbf{k}_j| = |\mathbf{k}'_j| = k$, and ϕ_j is the phase difference for beams in pair j. Since $|\mathbf{G}_j| = \sqrt{3}\,k$, the choice $|\mathbf{G}_j| = \pi/a$ implies $k = \pi/(\sqrt{3}a)$. In what follows, we use the $a = \pi/\sqrt{3}k$ as the length unit and recoil energy

$$E_\mathrm{r} = \frac{\hbar^2 k^2}{2m} = \frac{\pi^2\hbar^2}{6ma^2}, \quad (3)$$

as the energy unit. Unless stated otherwise, the zero of energy is taken to be the ground-state energy of the corresponding single-particle Hamiltonian $\hat{H}_0$ for the parameters (V_0, ϕ_g) under consideration. Note that we can restrict ourselves to $V_0 \geq 0$ since changing the sign of V_0 is equivalent to shifting each ϕ_j into $\phi_j + \pi$. The choice of the spatial origin provides two independent degrees of freedom, allowing two of the three phases to be absorbed by a coordinate shift. As a result, the geometry of the potential is determined by a single phase. Without loss of generality, we may choose the so-called *geometric phase* $\phi_\mathrm{g} = \sum_j \phi_j$ [36] and take $\phi_1 = \phi_2 = \phi_3 = \phi_\mathrm{g}/3$.

Irrespective of the value of ϕ_g, the potential $V(\mathbf{r})$ is periodic with Bravais vectors $\mathbf{a}_1 = (4a/\sqrt{3})\mathbf{e}_x$ and $\mathbf{a}_2 = (2a/\sqrt{3})(\mathbf{e}_x + \sqrt{3}\mathbf{e}_y)$, with $\mathbf{e}_x, \mathbf{e}_y$ the canonical basis of $\mathbb{R}^2$, see Fig. 1(b). For $\phi_\mathrm{g} = 0$, the potential minima form a honeycomb lattice with identical A and B sites, see Fig. 1(b). An increasing value of ϕ_g progressively lifts the degeneracy between A and B sites, hence forming an hBN-like potential. For $|\phi_\mathrm{g}| > \pi/2$, the B points are no longer local minima while the A sites are still minima, hence forming a triangular lattice, see Appendix A.

In the low-energy s-wave scattering regime, the interaction potential is characterized by the sole scattering length a_sc and, for weak enough interactions,

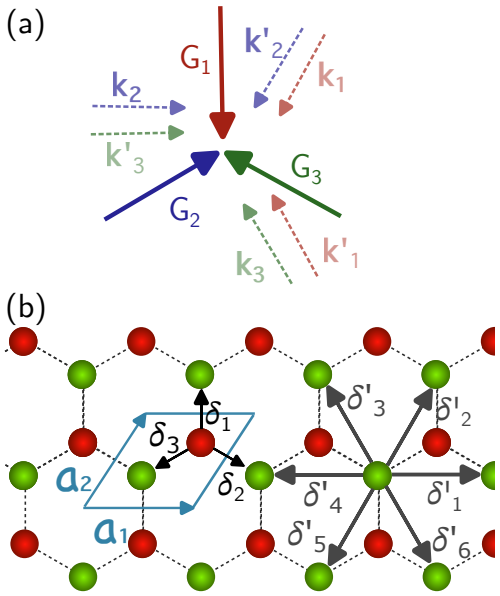

Figure 1. Hexagonal lattice. (a) Lattice vectors $\mathbf{G}_j$ entering the potential of Eq. (2). Faint arrows indicate the laser wave vectors in the implementation of Ref. [36]. (b) Lattice formed by the minima of the potential in Eq. (2). It is composed of two interpenetrating triangular sublattices A (red) and B (green). Also shown are the Bravais vectors $\mathbf{a}_{1,2}$, the nearest-neighbor vectors $\boldsymbol{\delta}_j$, and the next-nearest-neighbor vectors $\boldsymbol{\delta}'_j$.

$U(\mathbf{r})$ may be replaced by a contact interaction, $U(\mathbf{r}) = (\hbar^2\tilde{g}/m)\delta(\mathbf{r})$, with dimensionless coupling parameter

$$\tilde{g} \simeq \frac{1}{\tilde{g}_0^{-1} + (4\pi)^{-1}\ln(\Lambda E_\mathrm{r}/\mu)}, \quad (4)$$

where

$$\tilde{g}_0 = \frac{2\pi}{\ln(a/a_\mathrm{sc})}, \quad (5)$$

μ the chemical potential, and $\Lambda \simeq 0.423$ is a numerical constant[1] [14, 54–57]. This relation holds for homogeneous two-dimensional systems in the weakly-interacting regime $\tilde{g} \ll 1$ and is used here heuristically.

For sufficiently deep lattice potential, $V_0 \gg E_\mathrm{r}$, and low-energy, the system may be described, up to an irrelevant constant, by the extended Bose–Hubbard model

[1] With our convention $E_\mathrm{r} = \hbar^2k^2/2m = \pi^2\hbar^2/(6ma^2)$ the recoil-energy unit differs by a factor of 3 from the more common convention $E_\mathrm{r} = \pi^2\hbar^2/(2ma^2)$. Accordingly, the constant Λ in Eq. (4) is three times the value given in Refs. [14, 54–57].

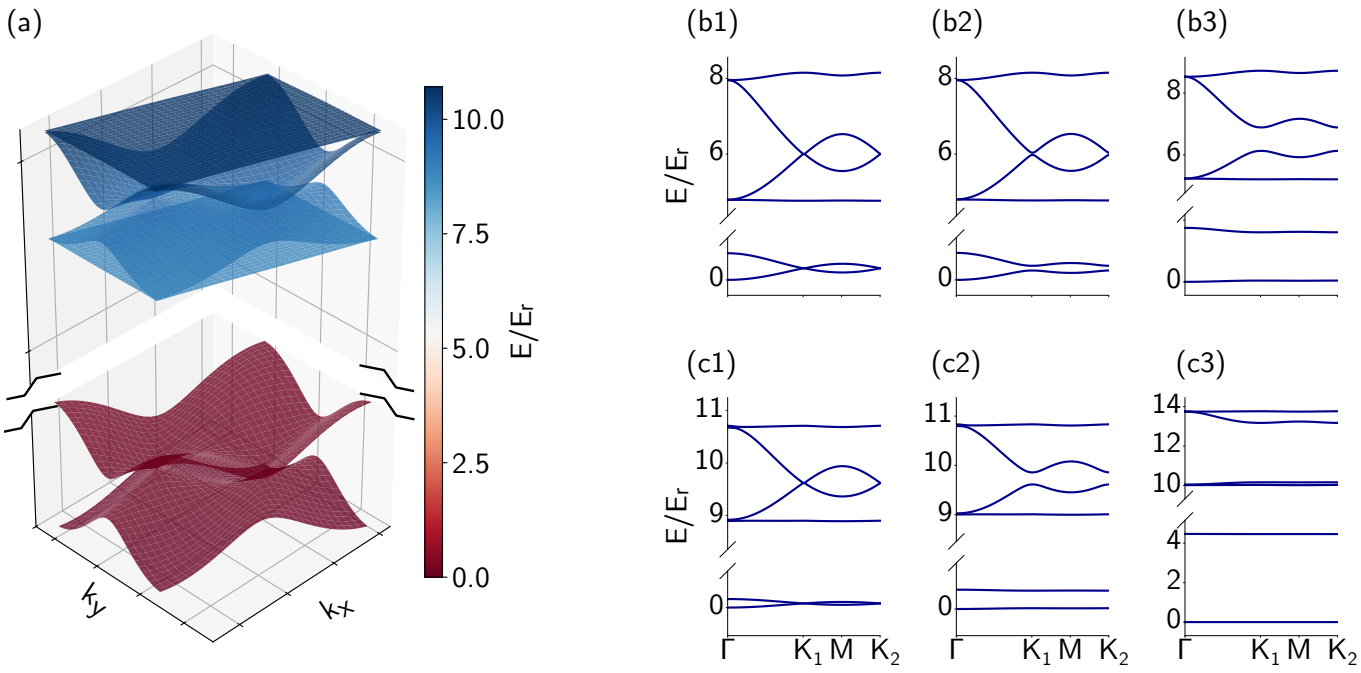

Figure 2. Single-particle band structure for a honeycomb potential with various amplitudes and geometric phases. Results obtained using exact diagonalization of Hamiltonian $\hat{H}_0$. (a) Full dispersion relations in the first Brillouin zone for the first bands, $V_0 = 15\,E_\mathrm{r}$, and $\phi_\mathrm{g} = 0$. (b1) Band dispersion relations along the high-symmetry path Γ–K_1–M–K_2 for $V_0 = 5\,E_\mathrm{r}$, and (b1) $\phi_\mathrm{g} = 0$, (b2) $\phi_\mathrm{g} = 0.008$, and (b3) $\phi_\mathrm{g} = 0.1$. (c) Same as (b) but for $V_0 = 15\,E_\mathrm{r}$.

(BHm) Hamiltonian

$$\begin{aligned}\hat{H}_{\mathrm{BH}} \;=\; & -J\sum_{\langle j,\ell\rangle}\hat{a}_j^\dagger\hat{a}_\ell - \frac{\Delta_{\mathrm{AB}}}{2}\sum_{j\in A}\hat{a}_j^\dagger\hat{a}_j + \frac{\Delta_{\mathrm{AB}}}{2}\sum_{j\in B}\hat{a}_j^\dagger\hat{a}_j \\ & -J'_{\mathrm{A}}\sum_{\langle\langle j,\ell\rangle\rangle\in A}\hat{a}_j^\dagger\hat{a}_\ell - J'_{\mathrm{B}}\sum_{\langle\langle j,\ell\rangle\rangle\in B}\hat{a}_j^\dagger\hat{a}_\ell \\ & +\frac{U_{\mathrm{A}}}{2}\sum_{j\in A}\hat{n}_j\left(\hat{n}_j-1\right) + \frac{U_{\mathrm{B}}}{2}\sum_{j\in B}\hat{n}_j\left(\hat{n}_j-1\right),\end{aligned} \tag{6}$$

where $\hat{a}_j$, $\hat{a}_j^\dagger$, and $\hat{n}_j = \hat{a}_j^\dagger\hat{a}_j$ are, respectively, the annihilation, creation, and number operators for bosons in site j, J is the tunneling energy between nearest-neighbor (nn) A-B sites, J'_A and J'_B are the tunneling energies between next-nearest-neighbor (nnn) A-A or B-B sites, $\Delta_{\mathrm{AB}} \geq 0$ is the energy difference between A and B sites (by convention we define A sites as those with lowest energy), and U_A and U_B are, respectively, the interaction energy in A and B sites. The notations $\langle j,\ell\rangle$ and $\langle\langle j,\ell\rangle\rangle$ refer to sums over pairs of nn A-B sites and pairs of nnn A-A or B-B sites, respectively.

III. BAND STRUCTURE AND TIGHT-BINDING PARAMETERS

We first study the single-particle part of Eq. (1), associated with the Hamiltonian $\hat{H}_0$. Using Bloch's theorem, $\hat{H}_0$ may be diagonalized writing the wavefunctions $\psi_{b,\mathbf{k}}(\mathbf{r}) = u_{b,\mathbf{k}}(\mathbf{r})e^{i\mathbf{k}\cdot\mathbf{r}}$, where $u_{b,\mathbf{k}}(\mathbf{r})$ has the lattice periodicity, $\mathbf{k}$ spans the first Brillouin zone, and b is the band index. The eigenproblem $\hat{H}_0\psi_{b,\mathbf{k}} = \varepsilon_b(\mathbf{k})\psi_{b,\mathbf{k}}$ is then solved, for given sets of V_0 and ϕ_g, using exact numerical diagonalization in continuous space within the first Brillouin zone. It yields the numerically exact band dispersion relations $\varepsilon_b(\mathbf{k})$ and the corresponding eigenstates $\psi_{b,\mathbf{k}}(\mathbf{r})$.

Typical energy spectra are shown in Fig. 2 for for various values of V_0 and ϕ_g. For deep enough potential, the lowest band ($b = 1$) can be understood from the tight-binding model (TBm) corresponding to the first two lines in Eq. (6), i.e. for $U_\mathrm{A} = U_\mathrm{B} = 0$. The latter has been extensively studied previously, see for instance Refs. [3, 48, 58, 59]. The lowest band splits into two subbands ($\pm$) with dispersion relations

$$\begin{aligned}\varepsilon_{1,\pm}(\mathbf{k}) \;=\; & \pm J\sqrt{|f(\mathbf{k})|^2 + \left[\frac{(J'_\mathrm{A}-J'_\mathrm{B})f'(\mathbf{k}) + \Delta_{\mathrm{AB}}}{2J}\right]^2} \\ & -\frac{J'_\mathrm{A}+J'_\mathrm{B}}{2}f'(\mathbf{k}),\end{aligned} \tag{7}$$

where $f(\mathbf{k}) = \sum_{j=1}^{3} e^{i\boldsymbol{\delta}_j\cdot\mathbf{k}}$ with $\boldsymbol{\delta}_j$ the lattice vectors connecting A-B pairs of nn sites and $f'(\mathbf{k}) = \sum_{j=1}^{3} e^{i\boldsymbol{\delta}'_j\cdot\mathbf{k}}$ with $\boldsymbol{\delta}'_j$ the lattice vectors connecting A-A or B-B pairs of nnn sites, see Fig. 1(b). Explicit formulas are given in Appendix B. The lowest band spectra we obtain for the continuous-space model are in good agreement with TBm predictions, Eq. (7), for typically $V_0 \gtrsim 5\,E_\mathrm{r}$

More precisely, the BHm parameters J, $J'_{\rm A}$, $J'_{\rm B}$, and $\Delta_{\rm AB}$ are extracted by fitting Eq. (7) to the lowest-band dispersion relation obtained numerically from the continuous model. Moreover, Wannier functions in A and B sites, $w_{\rm A}(\mathbf{r}-\mathbf{R}_j)$ and $w_{\rm B}(\mathbf{r}-\mathbf{R}_j)$ with $\mathbf{R}_j$ the position of site j, are obtained through a variational procedure that minimizes their real-space spread starting from the Bloch eigenstates [60]. The on-site interaction energies, useful for the many-body problem, are then computed as

$$U_{\rm A/B} = \tilde{g}\int d\mathbf{r}\,|w_{\rm A/B}(\mathbf{r})|^4. \tag{8}$$

Finally, the quality of the fits is assessed through the error parameter, defined as the average of the absolute value of the difference between the TB dispersion and the exact dispersion, normalized by the corresponding subband width:

$$\epsilon_\pm = \frac{1}{\mathcal{A}\,S_\pm}\int d\mathbf{k}\;\left|\varepsilon_{1,\pm}(\mathbf{k}) - \varepsilon^{\rm TB}_{1,\pm}(\mathbf{k})\right|, \tag{9}$$

where $\varepsilon_{1,\pm}(\mathbf{k})$ and $\varepsilon^{\rm TB}_{1,\pm}(\mathbf{k})$ are the dispersion relation, respectively, obtained by diagonalizing the continuous Hamiltonian and predicted by the TB model [Eq. (7) with fitted parameters], $\mathcal{A} = \frac{\pi^2\sqrt{3}}{2a^2}$ is the area of the first Brillouin zone, and $S_\pm$ is the bandwidth of the subband. This procedure allows us to extract the effective tunneling parameters and, at the same time, to assess the validity range of each model. Results for the lowest subbands are shown in Fig. 3 for the full TBm as well as for some approximate models (see below).

For $\phi_{\rm g} = 0$, we have $\Delta_{\rm AB} = 0$ and, for sufficiently deep lattices, the nnn terms can be neglected. We then recover the standard dispersion relations of graphene, $\varepsilon_{1,\pm}(\mathbf{k}) \simeq \pm J|f(\mathbf{k})|$, which exhibit characteristic Dirac cones at K_1 and K_2 with locally linear dispersion relations, see Fig. 2(a), (b1), and (c1). The latter are known to exist for almost any potential invariant under $2\pi/3$ rotation and possessing inversion symmetry ($\mathbf{r}\leftrightarrow-\mathbf{r}$); they are thus robust against the inclusion of nnn terms that respect such symmetry, as well as in continuous space [61]. They are also found in the second band ($b=2$). There, owing to the symmetries of the potential, each site hosts two degenerate first local excitations associated with two Wannier states. For this reason, the second band splits into four subbands, corresponding to the two degenerate excited orbitals on each of the two sublattices. In contrast, while the extreme subbands are strictly flat in the tight-binding model restricted to nearest neighbors [62], we find weak $\mathbf{k}$ dependence in the continuous model for finite lattice amplitude V_0, see Fig. 2(b1) and (c1).

For finite $\phi_{\rm g}$, the equivalence of the sublattices A and B is broken and a relative energy offset $\Delta_{\rm AB}$ between A and B sites appears. A band gap opens at the Dirac points, with local quadratic dispersion relations, while the bands and subbands progressively separate as $\phi_{\rm g}$ (hence $\Delta_{\rm AB}$) grows, see Fig. 2(b2), (b3), (c2), and (c3). Expanding the energy difference between the

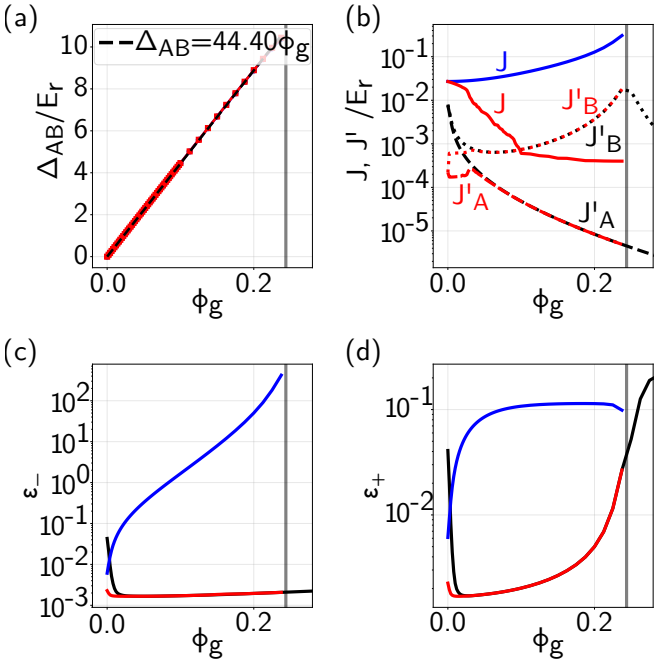

Figure 3. Tight-binding parameters as functions of the geometric phase $\phi_{\rm g}$ for $V_0 = 15\,E_{\rm r}$. Results obtained by fitting the lowest-band dispersion relation of the continuous single-particle Hamiltonian $\hat{H}_0$ to the nn (blue), nnn (red), and triangular (black) models. The vertical gray line marks $\phi^*_{\rm g} \simeq 0.25$, where the lowest B-site state crosses the first excited A-site state. (a) Sublattice offset $\Delta_{\rm AB}$ obtained from the nn (blue) and nnn (red) model (note that they overlap each other), together with a linear fit (dashed black line). (b) Tunneling amplitudes: J (solid), $J'_{\rm A}$ (dashed), and $J'_{\rm B}$ (dotted) for each model. (c) and (d) Normalized fitting errors for, respectively, the lower and upper subbands.

ground states of the harmonic approximations of the potential around A and B sites, we find that $\Delta_{\rm AB}$ grows linearly with $\phi_{\rm g}$, $\Delta_{\rm AB} \simeq (2\sqrt{3}V_0 - \sqrt{3V_0\,E_{\rm r}})\phi_{\rm g}$, see Appendix A. This is in good agreement with fits to our numerical results, $\Delta_{\rm AB}/E_{\rm r} \simeq 44.40\,\phi_{\rm g}$, see Fig. 3(a). The small discrepancy (less than 2%) may be attributed to the slight anharmonic effects. Owing to the smaller separation between pairs of sites, the nn overlaps of Wannier functions always dominate their nnn counterparts. For $\Delta_{\rm AB} \ll 3J$, where $3J$ sets the half-bandwidth of the nn honeycomb dispersion [$\varepsilon_{1,\pm}(\mathbf{k}) = \pm J|f(\mathbf{k})|$ and $|f(\mathbf{k})| \le 3$], we can rely on the nn model corresponding to neglecting the second line of Eq. (6), and the primed terms in Eq. (7). The dispersion relations then reduce to $\varepsilon_{1,\pm}(\mathbf{k}) \simeq \pm\frac{\sqrt{\Delta^2_{\rm AB}+4J^2|f(\mathbf{k})|^2}}{2}$. This is consistent with Fig. 3, where we find that the nn model remains accurate for small $\phi_{\rm g}$. A crossover occurs when $\Delta_{\rm AB} \sim 3J$, which for $V_0 = 15\,E_{\rm r}$ happens around $\phi_{\rm g} \simeq 0.002$. The transition between effective descriptions is, however, gradual: in the vicinity of this crossover, the fitting errors of both the nn and triangular models remain reasonably small ($\lesssim 2\%$), so that either model provides a useful de-

scription of the low-energy physics. For larger ϕ_g, nn tunneling becomes progressively off-resonant, while nnn tunneling remains resonant within each sublattice. The A and B sublattices then progressively decouple and the triangular-lattice description becomes more appropriate. The terms in J may be neglected and the dispersion relations, Eq. (7), reduce to $\varepsilon_{1,\pm}(\mathbf{k}) \simeq \pm\Delta_{AB}/2 \pm J'_{A/B} f'(\mathbf{k})$ where A corresponds to $-$ and B corresponds to $+$. This is consistent with Fig. 3, where we find that the tunnelings and errors obtained from the full (dotted and dashed red lines) and triangular (dotted and dashed black lines) models are similar for $\phi_g \gtrsim 0.025$, corresponding to $\Delta_{AB}/3J \gtrsim 20$ for $V_0 = 15\,E_r$. Finally, beyond a certain threshold, $\phi_g \gtrsim \phi_g^*$ (with $\phi_g^* \simeq 0.25$ for $V_0 = 15\,E_r$, vertical lines in Fig. 3), the energy offset Δ_{AB} exceeds the excitation energy on A sites, so that the ground-band Wannier state energy on B sites exceeds that of first excited states on A sites. Hence the only reasonable single-band TBm for the lowest subband considered here becomes the triangular one for A sites. Description of higher bands would involve including p-orbitals in A sites, s-orbitals in B sites, as well possibly there hybridation, which is beyond the scope of the present work.

IV. QUANTUM PHASE DIAGRAMS FOR INTERACTING BOSONS

We now turn to the many-body problem. Low-temperature equilibrium properties of the full model of Eq. (1) for the potential of Eq. (2) are found using worm-algorithm quantum path-integral Monte Carlo (PIMC) calculations [63]. We work within the grand-canonical ensemble with temperature T and chemical potential μ. The interaction term is treated using the generalized propagator parametrized by the scattering length a_{sc}, as introduced in Ref. [57]. Unless stated otherwise, all simulations are performed at lattice depth $V_0 = 15\,E_r$ and temperature $T = 0.01\,E_r/k_B$, within in a 6×6 unit-cell box with periodic boundary conditions, containing 72 local lattice sites. The observables extracted from our PIMC calculations are the local particle density $\rho(\mathbf{r}) = \langle \hat{\Psi}^\dagger(\mathbf{r})\hat{\Psi}(\mathbf{r})\rangle$, the average particle number per site (i.e. per half-unit cell) $n = \int d\mathbf{r}\,\rho(\mathbf{r})/N_c$, with N_c the number of half-unit cells in the simulation box, the average particle number in A and B sites, n_A and n_B [with $n = (n_A + n_B)/2$], the compressibility $\kappa = \partial n/\partial\mu$, and the superfluid fraction f_s. The first five are computed using the particle position statistics while the latter is computed using the winding number estimator [64]. Our PIMC computations are performed in continuous space and interpreted in terms of the extended hBN-like BHm Hamiltonian of Eq. (6).

A. Honeycomb lattice

We start with the balanced honeycomb lattice, $\phi_g = 0$. In this case, the two sublattices A and B are equivalent, $\Delta_{AB} = 0$, $U_A = U_B \equiv U$, and $J'_A = J'_B \equiv J'$. For $V_0 = 15\,E_r$, the single-particle results yield $J \simeq 2.7 \times 10^{-2}\,E_r$ and $J' \simeq 2.2 \times 10^{-4}\,E_r$, and the nnn tunneling can be neglected. The low-energy dynamics is thus essentially governed by the competition between onsite interactions U and nn tunneling J in Bose-Hubbard-like models. Typical PIMC results for the density per half unit cell n, the compressibility κ, and the superfluid fraction f_s are shown in Fig. 4(a) for various temperatures ranging from $T \simeq 0.3\,E_r/k_B$ (lighter blue) to $T \simeq 0.01\,E_r/k_B$ (darker blue). For sufficiently low temperatures, we clearly observe two Mott plateaus at integer fillings $n = 1$ and $n = 2$, corresponding to 1 and 2 particles per (A or B) site, with vanishing compressibility, and separated by compressible phases. This corresponds to SF-MI phase transitions. Consistently, we find that the SF fraction is finite in the compressible regions and vanishes in the Mott plateaus. Thermal fluctuations marginally affect the density and compressibility for $k_B T \lesssim 0.1\,E_r$, which is about one order of magnitude smaller than the interaction energy $U \simeq 1.83\,E_r$ for $\tilde{g}_0 \simeq 0.67$ as used for Fig. 4. The first MI gap at $n = 1$ is approximately equal to U as expected in the atomic limit $U \gg J$, while the second one is significantly reduced due to enhanced tunneling at $n \simeq 2$ (see below). In contrast, zero-temperature convergence of the SF fraction requires lower temperatures. For $k_B T \gtrsim 0.2\,E_r$, all superfluid phases are destroyed, while for $0.05\,E_r \lesssim k_B T \lesssim 0.2\,E_r$ (with $0.05\,E_r \simeq 2J$) only the first, low-density superfluid phase is suppressed. For low density, the relevant energy scale is the tunneling energy J and we consistently find a significant SF for $k_B T \lesssim J \simeq 2.7 \times 10^{-2}\,E_r$. The second and third SF phases are more stable, and we find that the SF fraction is converged for roughly $k_B T \lesssim J \simeq 0.1\,E_r$ in spite of fluctuations of the PIMC results for f_s. At higher temperatures, the SF phases found at zero temperature are replaced by normal-fluid (NF) phases, characterized by finite compressibility and vanishing SF fraction.

More precisely, in 2D, the NF to SF transition is expected to be of the Berezinskii-Kosterlitz-Thouless (BKT) type [65–67]. To check this, we study the superfluid phase-space density $n_s\lambda_T^2$ as a function of temperature T, where $n_s = f_s \times n$ is the superfluid density and $\lambda_T = \sqrt{2\pi\hbar^2/mk_B T}$ is the thermal de Broglie wavelength. A typical result for a fixed chemical potential μ is shown in Fig. 4(b) for various system sizes. The behavior shows a sharper and sharper transition as the size increases and a critical point consistent with the universal jump of the superfluid phase-space density at $n_s\lambda_T^2 = 4$, characteristics of the BKT transition. Here we find a critical temperature of $T_c \simeq 0.03\,E_r/k_B$. Hence, the temperature used for the phase diagrams discussed below, $T = 0.01\,E_r/k_B$, is low enough to be representative of zero-temperature behavior. Moreover, we find that, al-

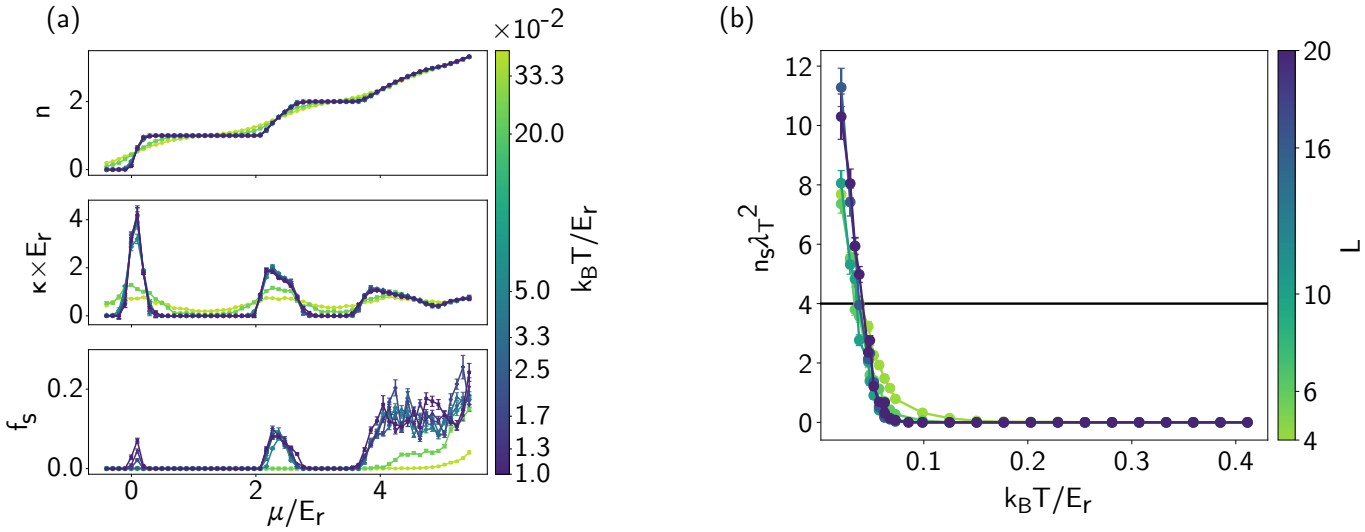

Figure 4. Quantum Monte Carlo simulation results for 2D bosons in a honeycomb optical lattice ($V_0 = 15\,E_\mathrm{r}$, $\phi_\mathrm{g} = 0$, $\tilde{g}_0 = 0.67$) for several temperatures and system sizes. (a) Density n, compressibility κ, and superfluid fraction f_s versus chemical potential for several temperatures (the ticks on the colorbar indicate the used temperatures). (b) Superfluid phase-space density $n_\mathrm{s}\lambda_T^2$ versus temperature for various system sizes $L \times L$ (indicated on te colorbar), for $\mu \simeq 2.17\,E_\mathrm{r}$. The black horizontal line indicates the expacted BKT superfluid transition.

though the superfluid density is not fully converged, a system of $L \times L$ unit cells with $L = 6$ is sufficient to locate the critical temperature clearly via the criterion $n_\mathrm{s}\lambda_{T_\mathrm{c}}^2 = 4$.

The phase diagram of the balanced honeycomb model shown in Fig. 5(a) is obtained by analyzing results as in Fig. 4(a) while varying the interaction strength $\tilde{g}_0$. At the used temperature, $T = 0.01\,E_\mathrm{r}/k_\mathrm{B}$, only very small regions exhibit finite compressibility and vanishing SF fraction, corresponding to a normal fluid (NF, dark green). The remainder of the diagram consists of two MI lobes with zero compressibility and zero SF fraction at integer fillings $n_A = n_B = 1$ ($\mathrm{MI}_{1,1}$, purple) and $n_A = n_B = 2$ ($\mathrm{MI}_{2,2}$, pink), surrounded by a broad SF phase (light green).

The critical interaction strength for the appearance of the MI lobes is $\tilde{g}_0 = 0.25 \pm 0.05$, corresponding to $U_\mathrm{c}/J = 15.2 \pm 3.0$ for $V_0 = 15\,E_\mathrm{r}$ as used in Fig. 5(a). This is comparable to BHm estimates for the honeycomb lattice, which yield $U_\mathrm{c}/J \simeq 11.6$, obtained from high-order process-chain expansions [51] and $U_\mathrm{c}/J \simeq 12.7$ from strong-coupling perturbation theory with series extrapolation [52]. While our continuous-space phase diagram is qualitatively similar to BHm predictions (MI lobes corresponding to the estimate of Ref. [51] are shown as thin dashed lines), it exhibits clear quantitative deviations. The MI lobe at $n_A = n_B = 1$ agrees well up to an approximate shift of the chemical potential of order $\Delta\mu = 0.15\,E_\mathrm{r}$. In contrast, the MI lobe at $n_A = n_B = 2$ exhibits a gap that is approximately half the size predicted by the BHm. Furthermore, the MI lobe at $n_A = n_B = 3$ predicted by the BHm is completely absent from the full continuous-space PIMC calculations. In fact, the PIMC results show a weak inflection point of the $n(\mu)$ curve at $n = 3$, but the compressibility and the SF fraction remain finite, see Fig. 4(a). This indicates enhanced correlations, but not strong enough to stabilize a MI phase. These deviations, in particular the suppression of the $n = 2$ lobe and the absence of the $n = 3$ lobe, indicate that the BHm fails to completely capture the low-energy physics in this regime, highlighting the need for continuous-space calculations.

To explain these discrepancies, we may consider corrections to the standard BHm. We first note that the higher single-particle bands, which appear at energies around $8.75\,E_\mathrm{r}$ for $V_0 = 15\,E_\mathrm{r}$, see Fig. 2(c1), lie well above the chemical-potential range considered in the phase diagram of Fig. 5(a) and can therefore be ignored. We may then consider nnn tunneling terms, corresponding to the second line of Eq. (6), as well as nn interactions, which generate a term of the form $\frac{U'}{2}\sum_{\langle j,\ell\rangle}\hat{n}_j\hat{n}_\ell$, where $U' = \tilde{g}\int d\mathbf{r}\,|w_\mathrm{A}|^2|w_\mathrm{B}|^2$. Such terms are expected to play a role for shallow lattices owing to enhanced spatial extension of the Wannier functions. For $V_0 = 15\,E_\mathrm{r}$ as used here, however, our single-particle calculations yield $J' \simeq 2.18 \times 10^{-4}\,E_\mathrm{r}$ and $U'/\tilde{g} \simeq 1.9 \times 10^{-4}\,E_\mathrm{r}$. These terms are, respectively, about two and four orders of magnitude smaller than the nn tunneling ($J \simeq 2.7 \times 10^{-2}\,E_\mathrm{r}$) and on-site interaction strength ($U/\tilde{g} \simeq 2.73\,E_\mathrm{r}$), and can safely be neglected. In contrast, density-assisted tunneling (DAT), which arises from nn coupling terms, $-\tilde{J}\sum_{\langle j,\ell\rangle}\hat{a}_j^\dagger(\hat{n}_j + \hat{n}_\ell)\hat{a}_\ell$ with $\tilde{J} = -\tilde{g}\int d\mathbf{r}\,|w_\mathrm{A}|^2 w_\mathrm{A}^* w_\mathrm{B}$, becomes significant. Such terms are beyond BHm. Nevertheless, we may estimate their significance within a mean-field approach by replacing the density operator $\hat{n}_j + \hat{n}_\ell$ by its average value $2n$. We then recover the

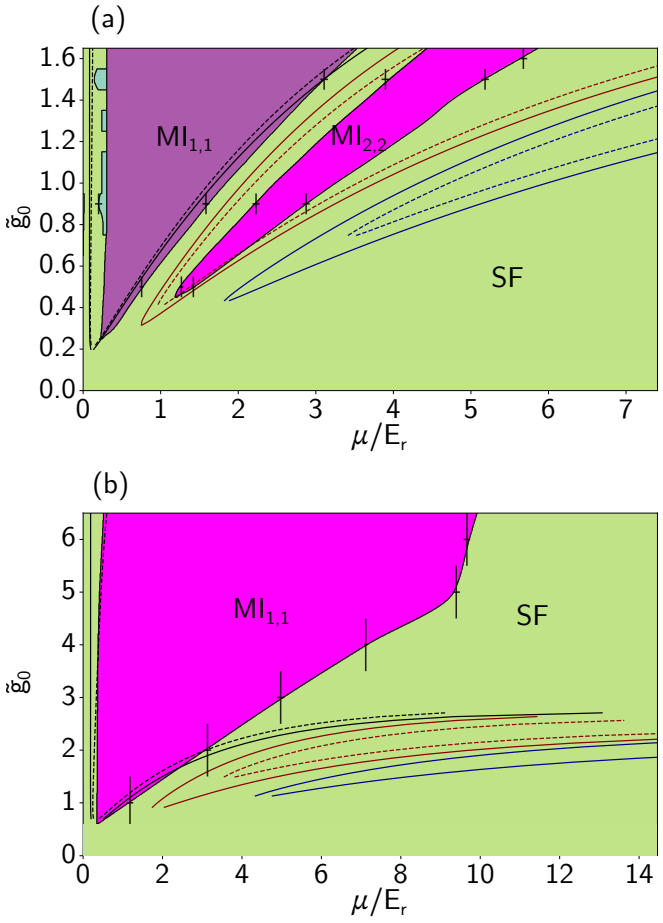

Figure 5. Quantum phase diagram for bosons in the honeycomb lattice ($\phi_g = 0$) versus chemical potential and interaction strength for (a) $V_0 = 15\,E_r$ and (b) $V_0 = 9.75\,E_r$ Results obtained using continuous-space QMC for $k_BT = 0.01\,E_r$, Colored regions denote superfluid (light green), normal-fluid (dark green), and Mott insulator (purple-mauve) phases. The crosses indicate selected boundary points obtained numerically with error bars corresponding to $\tilde{g}_0$–μ space discretization; only a subset is shown for visual clarity. Phase boundaries (solid black lines) are obtained by interpolation and extrapolation consistent with these error bars. Colored lines show Mott lobes predicted by the Bose–Hubbard model, from Ref. [51] using the nn tunneling extracted as in Fig. 3(b) (solid lines) and including DAT corrections ($J \to J + 2n\tilde{J}$, dashed lines).

BHm where the hopping energy J must be replaced by the effective hopping energy $J + 2n\tilde{J}$. Here, $\tilde{J}$ is evaluated using the bare coupling $\tilde{g}_0$; since in most of the relevant parameter range $\tilde{g} > \tilde{g}_0$, this provides a conservative estimate of DAT effects. Examination of this term shows that the mean-field DAT correction is on the order of 30% near the center of the Mott lobe at $n = 1$, on the order of 70% in the lobe at $n = 2$, and on the order of 100% in the lobe at $n = 3$, see Appendix D. The Mott lobes estimated from BHm predictions and including the mean-field DAT corrections are shown as dashed lines in the phase diagrams of Fig. 5. These results show that, while the MI lobe at $n = 1$ is marginally affected, the lobes at $n = 2$ and $n = 3$ are strongly reduced. This suggests that DAT terms are important, even for a large lattice depth such as $V_0 = 15\,E_r$. The simple mean-field treatment used here is qualitatively consistent with our PIMC results. Quantitative agreement, particularly the complete disappearance of the lobe at $n = 3$, would, however, require a full quantum treatment of the DAT terms, which is beyond the BHm.

As expected, the breakdown of the BHm becomes more pronounced for shallower lattices. Fig. 5(b) shows the phase diagram for the same system at $V_0 = 9.75\,E_r$. Qualitatively, the situation remains similar to the case at $V_0 = 15\,E_r$, but with significantly stronger deviations from the BHm description. First, density-assisted tunneling (DAT) effects are enhanced in shallower lattices due to the increased spatial extent of the Wannier functions, leading to a larger relative correction to the bare tunneling amplitude. Second, the relevant chemical potentials now extend beyond the gap separating the lowest band from the first excited band. In particular, the first Mott lobe is stabilized at chemical potentials exceeding this gap, signaling that higher-band processes already play a role at unit filling. Third, the effective interaction description based on Eq. (4) is no longer a good heuristic in this regime. That expression relies on the assumption of sufficiently small $\tilde{g}_0$ and μ, whereas the parameters considered here lie outside this perturbative regime. Taken together, these three effects lead to substantial deviations from the single-band BHm at $V_0 = 9.75\,E_r$.

B. Hexagonal boron nitride lattice

We finally consider the asymmetric case, where $\phi_g \neq 0$. This case was studied for unit filling, $n_A + n_B = 2$, in Ref. [53], where it was shown that competition between the energy offset Δ_{AB} and on-site interaction energy induces transitions from SF to $MI_{1,1}$ and $MI_{2,0}$ phases. Beyond unit filling, we find a very rich phase diagram, shown in Fig. 6 for $V_0 = 15\,E_r$ and $\phi_g = \pi/30$, corresponding to $\Delta_{AB} \simeq 4.7\,E_r$, and $k_BT \simeq 0.01\,E_r$. Each colored region represents a SF (light green), a NF (dark green), and distinct Mott phases, labeled by the integer occupations (n_A, n_B) of the two sublattices.

The overall structure of the phase diagram in Fig. 6 can be qualitatively understood from the atomic limit $(J, J'_A, J'_B \to 0)$ of the extended BHm of Eq. (6). For $U_A \ll \Delta_{AB}$ and $\mu < \Delta_{AB}$, only the A sites are occupied and a series of $(n_A, 0)$ Mott plateaus appear as μ increases until $n_A U_A \simeq \Delta_{AB}$ or n_A is too large to stabilize a Mott insulator against Bose-enhanced tunneling. In both cases, the B sites are completely irrelevant for the MI phases. Because the relevant tunneling in this regime is the small next-nearest-neighbor term J'_A, the SF windows between MI plateaus are extremely narrow. More-

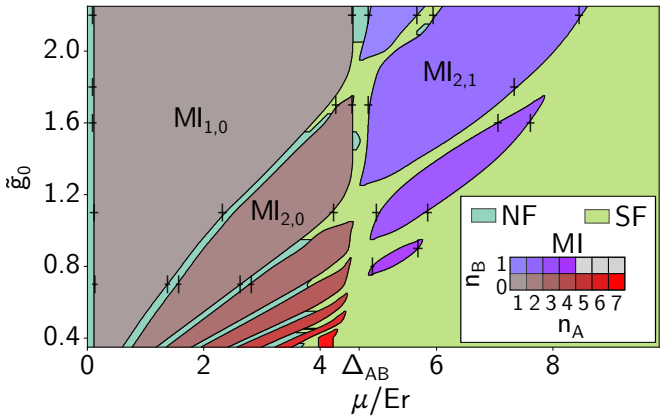

Figure 6. Quantum phase diagram for bosons in the asymmetric h-BN lattice with $\phi_g = \pi/30$ and $V_0 = 15\,E_r$ (corresponding to $\Delta_{AB} \simeq 4.7\,E_r$) versus chemical potential and interaction strength. Results obtained using continuous-space QMC for $k_B T = 0.01\,E_r$. Colored regions denote superfluid (light green), normal fluid (dark green), and Mott insulator (red, brown, purple; labeled by the sublattice occupations MI_{n_A,n_B}) phases. The crosses indicate selected boundary points obtained numerically with error bars corresponding to $\tilde{g}_0$–μ space discretization; only a subset is shown for visual clarity. Phase boundaries (solid black lines) are obtained by interpolation and extrapolation consistent with these error bars.

over, superfluidity would require a temperature typically smaller than J'_A, which is about two orders of magnitude smaller than our working temperature and we consistently find a NF phase. This behavior is observed in the phase diagram for $\tilde{g}_0 \in [0.24, 0.43]$, where the system effectively behaves as a weakly coupled triangular lattice on the A sublattice.

As $\tilde{g}_0$ increases, the onsite interaction U_A grows and the condition $\Delta_{AB} \simeq n_A U_A$ is reached. At this point, the B sites start to populate, giving rise to the sequence of Mott lobes $(n_A, 0) \rightarrow (n_A{+}1, 1)$, accompanied by broad SF regions between the Mott lobes. This regime is clearly visible in the ranges $\tilde{g}_0 \in [0.49, 0.55]$, $\tilde{g}_0 \in [0.67, 0.73]$, and $\tilde{g}_0 \in [1.09, 1.16]$. When $(n_A{-}1)U_A < \Delta_{AB} < n_A U_A$, the sequence changes to $(n_A, 0) \rightarrow (n_A, 1)$, as observed for $\tilde{g}_0 \simeq 0.61$ and $\tilde{g}_0 \in [0.73, 1.03]$. The behavior discussed in Ref. [53] for unit filling, corresponds to two transitions from $MI_{2,0}$ to SF and from SF to $MI_{1,1}$ observed in our diagram for $\mu \simeq \Delta_{AB}$ and $\tilde{g}_0 \in [1.06, 1.18]$. Note that for $\mu \gtrsim \Delta_{AB}$, the relevant tunnelings is J corresponding to hopping between nn A and B sites. It is larger than our working temperature and we consistently find SF regions instead of NF regions.

V. CONCLUSIONS

In this work, we have investigated the dynamics of ultracold bosons in honeycomb and h-BN-like optical potentials, combining continuous-space band structure calculations with exact QMC simulations. Our results reveal complex phase diagram, which may significantly deviate from the predictions of the standard BH model, even in regimes where single-particle properties are accurately described by tight-binding approximations. For the honeycomb lattice, we find that density-assisted tunneling, beyond the Bose-Hubbard frameworks, plays a crucial role, suppressing higher-order Mott insulator lobes and reshaping the phase boundaries. In the asymmetric h-BN lattice, the interplay between sublattice energy offset, tunneling, and interactions gives rise to a cascade of Mott insulator lobes with a variety of sublattice occupations, as well as broad superfluid domains. These findings underscore the importance of continuous-space approaches for accurately capturing the many-body physics of bosons in hexagonal lattices, particularly in regimes where beyond-nearest-neighbor tunneling and interaction-induced corrections become significant. These conclusions are in line with previous work in other nonstandard geometries, such as quasicrystal [57, 68, 69] and twisted potentials [70]. The rich phenomenology uncovered here invites further theoretical and experimental investigations, with potential implications for quantum simulation and the design of novel synthetic materials in hexagonal geometries. Our work not only provides a guide for future experiments with ultracold atoms or cavity polaritons in hexagonal potentials but also opens new avenues for exploring exotic quantum matter in other configurations, including superlattices, frustrated models, and multilayer systems.

ACKNOWLEDGMENTS

We thank Yifei Wang for early-stage contributions to the formulation of the single-particle problem. This work was supported by the Agence Nationale de la Recherche under projects QuanTEdu-France (ANR-CMAQ-002 France 2030) and QUTISYM (ANR-23-PETQ-0002), and by computing HPC and storage resources by GENCI at TGCC under the grants AD010510300R2 and AP010510288.

Appendix A: Geometry of the minima as a function of the geometric phase

In this Appendix, we analyze the extrema of the lattice potential as a function of the geometric phase ϕ_g. This determines the positions of the lattice sites used in the main text, the range of ϕ_g for which the potential contains two minima per unit cell, and the point at which only one minimum per lattice site is left and the lattice geometry reduces to a triangular one. We also derive the small-ϕ_g expression for the sublattice offset Δ_{AB}.

We consider the potential of Eq. (2) with $\phi_1 = \phi_2 = \phi_3 = \phi_g/3$. As in Fig. 1(a) of the main text, we orient

the reciprocal vectors as

$$\begin{cases} \mathbf{G}_1 = -\dfrac{\pi}{a}\mathbf{e}_y, \\ \mathbf{G}_2 = \dfrac{\pi}{a}\left(\dfrac{\sqrt{3}}{2}\mathbf{e}_x + \dfrac{1}{2}\mathbf{e}_y\right), \\ \mathbf{G}_3 = \dfrac{\pi}{a}\left(-\dfrac{\sqrt{3}}{2}\mathbf{e}_x + \dfrac{1}{2}\mathbf{e}_y\right). \end{cases} \tag{A1}$$

Introducing the variables

$$\theta_j = \mathbf{G}_j \cdot \mathbf{r}, \tag{A2}$$

and using $\mathbf{G}_1 + \mathbf{G}_2 + \mathbf{G}_3 = 0$, the potential depends on two independent variables only,

$$V(\theta_1, \theta_2) = 2V_0\Big[\cos(\theta_1 + \phi_g/3) + \cos(\theta_2 + \phi_g/3) + \cos(\theta_1 + \theta_2 - \phi_g/3)\Big]. \tag{A3}$$

It is sufficient to restrict the analysis to one unit cell, $\theta_{1,2} \in [0, 2\pi)$ and take $\phi_g \in (-\pi, \pi]$.

1. Stationary points and classification

The potential extrema satisfy

$$\begin{cases} \partial_{\theta_1} V \propto \sin(\theta_1 + \phi_g/3) + \sin(\theta_1 + \theta_2 - \phi_g/3) = 0, \\ \partial_{\theta_2} V \propto \sin(\theta_2 + \phi_g/3) + \sin(\theta_1 + \theta_2 - \phi_g/3) = 0. \end{cases} \tag{A4}$$

Subtracting the two equations gives

$$\sin(\theta_1 + \phi_g/3) = \sin(\theta_2 + \phi_g/3), \tag{A5}$$

which yields two branches of stationary points:

$$\begin{cases} \text{Branch A: } \theta_1 = \theta_2 \\ \text{Branch B: } \theta_2 = \pi - \theta_1. \end{cases} \tag{A6}$$

For Branch A, setting $\theta_1 = \theta_2 \equiv \theta$, the stationarity condition A4 becomes

$$\sin(\theta + \phi_g/3) + \sin(2\theta - \phi_g/3) = 0. \tag{A7}$$

Using trigonometric identities, this yields two families of solutions:

$$\theta = \frac{2\pi n}{3} \quad \text{with} \quad n = 0, 1, 2, \tag{A8}$$

and

$$\theta = \pi + \frac{2\phi_g}{3}. \tag{A9}$$

For Branch B, the solutions are

$$(\theta_1, \theta_2) = (\pi, 0), \qquad \left(2\pi - \frac{2\phi_g}{3}, \frac{2\phi_g}{3} - \pi\right). \tag{A10}$$

We now determine the nature of the stationary points from the Hessian matrix

$$H_{j\ell} = \frac{\partial^2 V}{\partial\theta_j \partial\theta_\ell}. \tag{A11}$$

For all Branch B solutions, as well as for the Branch A solution of Eq. (A9) one finds $\det H \leq 0$, so that these points are saddle points.

For the three Branch A solutions of Eq. (A8) the Hessian matrix reads

$$H = -2V_0 \begin{pmatrix} 2c_n & c_n \\ c_n & 2c_n \end{pmatrix}, \quad c_n = \cos\left(\frac{\phi_g}{3} + \frac{2\pi n}{3}\right). \tag{A12}$$

Hence, we find

$$\det H = 12V_0^2 c_n^2 \geq 0 \quad \text{and} \quad \operatorname{Tr} H = -12V_0 c_n, \tag{A13}$$

so that these points are minima when $c_n < 0$ and maxima when $c_n > 0$. This implies that the stationary point with $n = 0$ is always a maxima for any value of ϕ_g in our considered range and only $n = 1$ and $n = 2$ rest as candidate minima. In summary, among all stationary points, only those of the Branch A given by Eq. (A8) with $n = 1$ or $n = 2$ can be minima.

2. Number and position of the minima

The sign of

$$c_n = \cos\left(\frac{\phi_g}{3} + \frac{2\pi n}{3}\right) \tag{A14}$$

determines how many minima are present.

- For $|\phi_g| < \pi/2$, both $n = 1$ and $n = 2$ are minima. The lattice therefore contains two potential minima (lattice sites) per unit cell. For $\phi_g = 0$, the two sites are degenerate in energy and form the balanced honeycomb lattice. For $\phi_g \neq 0$, the degeneracy is lifted, yielding the imbalanced geometry discussed in the main text.
- For $|\phi_g| > \pi/2$, only one minimum remains corresponding to $n = 1$ for $\phi_g > 0$ and to $n = 2$ for $\phi_g < 0$. The lattice then reduces to a triangular lattice.

To find the positions of the minima, we solve Eq. (A2)

$$\theta_1 = \theta_2 = \frac{2\pi n}{3} \quad \text{with} \quad \begin{cases} n = 1 \\ n = 2\ . \end{cases} \tag{A15}$$

With the orientation of Fig. 1(a) of the main text, we find the real-space positions

$$\mathbf{r}_1 = \frac{2a}{\sqrt{3}}\mathbf{e}_x - \frac{2a}{3}\mathbf{e}_y, \qquad \mathbf{r}_2 = \frac{4a}{\sqrt{3}}\mathbf{e}_x - \frac{4a}{3}\mathbf{e}_y. \tag{A16}$$

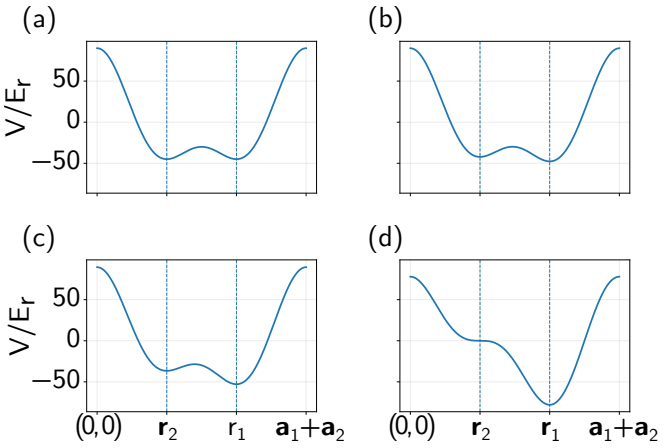

Figure 7. Line cut of the lattice potential at $V_0 = 15\,E_\mathrm{r}$ along the path $(0,0) \to \mathbf{r}_2 \to \mathbf{r}_1 \to \mathbf{a}_1 + \mathbf{a}_2$, for (a) $\phi_\mathrm{g} = 0$, (b) $\phi_\mathrm{g} = \pi/30$, (c) $\phi_\mathrm{g} = \pi/10$, and (d) $\phi_\mathrm{g} = \pi/2$. The dashed vertical lines mark the positions of $\mathbf{r}_2$ and $\mathbf{r}_1$.

Remarkably, these positions are independent of the geometric phase for the choice $\phi_1 = \phi_2 = \phi_3 = \phi_\mathrm{g}/3$.

For $\phi_\mathrm{g} > 0$, the $n = 1$ site is lower in energy and is identified with the A sublattice, while the $n = 2$ site corresponds to the B sublattice. For $\phi_\mathrm{g} < 0$, the roles are exchanged. To visualize the evolution of these extrema, Fig. 7 shows a one-dimensional cut of the potential taken along the line connecting $(0,0)$, $\mathbf{r}_2$, $\mathbf{r}_1$, and $\mathbf{a}_1 + \mathbf{a}_2$. For $\phi_\mathrm{g} = 0$, the two minima are degenerate, see Fig. 7(a). Increasing to $\phi_\mathrm{g} = \pi/30$ and to $\phi_\mathrm{g} = \pi/10$ lifts this degeneracy, see Figs. 7(b) and (c). Finally, for $|\phi_\mathrm{g}| = \pi/2$ one of the minima disappears, consistently with the transition to a triangular lattice, see Fig. 7(d).

3. Energy splitting and sublattice offset

We now focus on the regime $|\phi_\mathrm{g}| < \pi/2$, where the both extrema $n = 1, 2$ are local minima. The offset Δ_AB between the two sublattices has two contributions. The first one comes from the different values of the potential at the two minima. The second one comes from the different local curvatures of the wells, which yield different ground-state energies for the corresponding local harmonic oscillators.

The potential energy at each of the two minima is given by Eq. (A3) with

$$\theta_1 = \theta_2 = \frac{2\pi n}{3} \quad \text{and} \quad n = 1, 2, \tag{A17}$$

which yields

$$V_n = 6V_0 \cos\left(\frac{\phi_\mathrm{g}}{3} + \frac{2\pi n}{3}\right). \tag{A18}$$

The classical contribution to the energy splitting is thus

$$\begin{aligned}\Delta V &= V_2 - V_1 \\ &= 6V_0 \left[\cos\left(\frac{\phi_\mathrm{g}}{3} + \frac{4\pi}{3}\right) - \cos\left(\frac{\phi_\mathrm{g}}{3} + \frac{2\pi}{3}\right)\right].\end{aligned} \tag{A19}$$

Using trigonometric identities, we then find

$$\Delta V = 6\sqrt{3}\, V_0 \sin\left(\frac{\phi_\mathrm{g}}{3}\right). \tag{A20}$$

For $|\phi_\mathrm{g}| \ll 1$, it yields

$$\Delta V \simeq 2\sqrt{3}\, V_0\, \phi_\mathrm{g}. \tag{A21}$$

This is the splitting between the local potential minima.

To find the energy offset, we now include the harmonic zero-point contribution. Expanding the potential to quadratic order around a minimum $\mathbf{r}_n$ gives

$$V(\mathbf{r}) \simeq V_n + \frac{1}{2} \sum_{\alpha,\beta=x,y} H^{(n)}_{\alpha\beta}\, \delta r_\alpha \delta r_\beta, \tag{A22}$$

where

$$H^{(n)}_{\alpha\beta} = \left.\frac{\partial^2 V}{\partial\alpha\partial\beta}\right|_{\mathbf{r}=\mathbf{r}_n} \tag{A23}$$

is the Cartesian Hessian matrix. For the minima considered here, the Cartesian Hessian is diagonal,

$$H^{(n)}_{\alpha\beta} = -\frac{3\pi^2}{a^2} V_0 c_n\, \delta_{\alpha\beta}. \tag{A24}$$

The local harmonic frequency such that $V(\mathbf{r}_n + \delta\mathbf{r}) \approx V_n + m\omega_n^2(\delta\mathbf{r})^2/2$ is therefore

$$\omega_n^2 = -\frac{3\pi^2}{ma^2} V_0 c_n. \tag{A25}$$

Using the recoil-energy convention of the main text, $E_\mathrm{r} = \pi^2\hbar^2/6ma^2$, this may be written as

$$\omega_n = \frac{1}{\hbar}\sqrt{18 V_0 E_\mathrm{r}(-c_n)}\,. \tag{A26}$$

Since the local harmonic oscillator is two-dimensional and isotropic, the local zero point (zp) energy above the potential minimum V_n is $E^{(n)}_\mathrm{zp} = \hbar\omega_n$, that is,

$$E^{(n)}_\mathrm{zp} = \sqrt{18 V_0 E_\mathrm{r}}\sqrt{-c_n}. \tag{A27}$$

Expanding for $\phi_\mathrm{g} \ll 1$, we find

$$c_{1,2} = -\frac{1}{2} \mp \frac{\sqrt{3}}{6}\phi_\mathrm{g} + O(\phi_\mathrm{g}^2), \tag{A28}$$

where the upper sign corresponds to $n = 1$ and the lower sign to $n = 2$, and we obtain

$$\sqrt{-c_2} - \sqrt{-c_1} = -\frac{\sqrt{3}}{3\sqrt{2}}\phi_\mathrm{g} + O(\phi_\mathrm{g}^2). \tag{A29}$$

The zero-point contribution to the splitting is therefore

$$E_{\rm zp}^{(2)} - E_{\rm zp}^{(1)} = -\sqrt{3V_0 E_{\rm r}}\,\phi_{\rm g} + O(\phi_{\rm g}^2). \tag{A30}$$

Combining Eqs. (A21) and (A30), the energy difference between the two lowest local states in A and B sites is thus

$$\Delta_{\rm AB} = \left(2\sqrt{3}\,V_0 - \sqrt{3V_0 E_{\rm r}}\right)\phi_{\rm g}\ , \tag{A31}$$

to lowest order in $\phi_{\rm g}$.

Appendix B: Tight-binding models

In this Appendix, we give the explicit tight-binding conventions used in the main text. We first specify the lattice vectors and hopping geometry, then write the corresponding single-particle tight-binding Hamiltonian and dispersion relation. We finally give the nearest-neighbor and triangular limits used to analyze and fit band structures.

1. Lattice vectors and hopping geometry

We recall the Bravais vectors used in the main text,

$$\mathbf{a}_1 = \frac{4a}{\sqrt{3}}\,\mathbf{e}_x, \qquad \mathbf{a}_2 = \frac{2a}{\sqrt{3}}\,\mathbf{e}_x + 2a\,\mathbf{e}_y. \tag{B1}$$

The nearest-neighbor vectors connecting an A site to the three neighboring B sites, see Fig. 1(b), are

$$\begin{cases} \boldsymbol{\delta}_1 &= \frac{-\mathbf{a}_1+2\mathbf{a}_2}{3} = \frac{4a}{3}\,\mathbf{e}_y, \\ \boldsymbol{\delta}_2 &= \frac{2\mathbf{a}_1-\mathbf{a}_2}{3} = \frac{2a\sqrt{3}}{3}\,\mathbf{e}_x - \frac{2a}{3}\,\mathbf{e}_y, \\ \boldsymbol{\delta}_3 &= -\frac{\mathbf{a}_1+\mathbf{a}_2}{3} = -\frac{2a\sqrt{3}}{3}\,\mathbf{e}_x - \frac{2a}{3}\,\mathbf{e}_y. \end{cases} \tag{B2}$$

The next-nearest-neighbor vectors connect sites within the same triangular sublattice. We use the independent set

$$\begin{cases} \boldsymbol{\delta}'_1 &= \mathbf{a}_1 = \frac{4a}{\sqrt{3}}\,\mathbf{e}_x, \\ \boldsymbol{\delta}'_2 &= \mathbf{a}_2 = \frac{2a}{\sqrt{3}}\,\mathbf{e}_x + 2a\,\mathbf{e}_y, \\ \boldsymbol{\delta}'_3 &= \mathbf{a}_2 - \mathbf{a}_1 = -\frac{2a}{\sqrt{3}}\,\mathbf{e}_x + 2a\,\mathbf{e}_y, \end{cases} \tag{B3}$$

with the opposite vectors included implicitly in the next-nearest-neighbor sums.

2. Single-particle tight-binding Hamiltonian

Neglecting interactions, the tight-binding Hamiltonian associated with Eq. (6) reads as

$$\begin{aligned} \hat{H}_{\rm sp} \;=\; & -J\sum_{\langle j,\ell\rangle}\hat{a}_j^\dagger\hat{a}_\ell - \frac{\Delta_{\rm AB}}{2}\sum_{j\in A}\hat{a}_j^\dagger\hat{a}_j + \frac{\Delta_{\rm AB}}{2}\sum_{j\in B}\hat{a}_j^\dagger\hat{a}_j \\ & -J'_{\rm A}\sum_{\langle\langle j,\ell\rangle\rangle\in A}\hat{a}_j^\dagger\hat{a}_\ell - J'_{\rm B}\sum_{\langle\langle j,\ell\rangle\rangle\in B}\hat{a}_j^\dagger\hat{a}_\ell\,, \end{aligned} \tag{B4}$$

corresponding to the frist two lines of of Eq. (6) in the main text. After Fourier transformation, the nearest-neighbor and next-nearest-neighbor contributions are expressed in terms of the form factors

$$\begin{cases} f(\mathbf{k}) = \sum_{j=1}^{3} e^{i\mathbf{k}\cdot\boldsymbol{\delta}_j}, \\ f'(\mathbf{k}) = \sum_{j=1}^{3}\left(e^{i\mathbf{k}\cdot\boldsymbol{\delta}'_j} + e^{-i\mathbf{k}\cdot\boldsymbol{\delta}'_j}\right) = 2\sum_{j=1}^{3}\cos\!\left(\mathbf{k}\cdot\boldsymbol{\delta}'_j\right). \end{cases} \tag{B5}$$

Diagonalizing the resulting two-sublattice Hamiltonian gives

$$\begin{aligned} \varepsilon_{1,\pm}(\mathbf{k}) \;=\; & \pm J\sqrt{|f(\mathbf{k})|^2 + \left[\frac{(J'_{\rm A}-J'_{\rm B})f'(\mathbf{k}) + \Delta_{\rm AB}}{2J}\right]^2} \\ & -\frac{J'_{\rm A}+J'_{\rm B}}{2}f'(\mathbf{k})\,, \end{aligned} \tag{B6}$$

i.e., Eq. (7). This is the expression used in the fits of the lowest two subbands for the next nearest neighbor (nnn) model.

3. Limiting models: nearest neighbor and triangular

a. Nearest neighbor model. The nearest-neighbor (nn) model is obtained by setting $J'_{\rm A} = J'_{\rm B} = 0$. Eq. (B6) then reduces to

$$\varepsilon_{\pm}^{\rm nn}(\mathbf{k}) = \pm\frac{1}{2}\sqrt{\Delta_{\rm AB}^2 + 4J^2|f(\mathbf{k})|^2}. \tag{B7}$$

In this regime, for $\Delta_{\rm AB} = 0$, one recovers the balanced honeycomb dispersion relation

$$\varepsilon_{1,\pm}(\mathbf{k}) = \pm J|f(\mathbf{k})|. \tag{B8}$$

b. Triangular model. For a large energy offset, the two sublattices effectively decouple. This is exact for $J = 0$, and it is also obtained perturbatively for $\Delta_{\rm AB} \gg J|f(\mathbf{k})|$. Expanding Eq. (B6) in this regime gives

$$\begin{aligned} \varepsilon_{\rm A}(\mathbf{k}) &= -\frac{\Delta_{\rm AB}}{2} - J'_{\rm A}f'(\mathbf{k}) + \mathcal{O}\!\left(\frac{J^2}{\Delta_{\rm AB}}\right), \\ \varepsilon_{\rm B}(\mathbf{k}) &= +\frac{\Delta_{\rm AB}}{2} - J'_{\rm B}f'(\mathbf{k}) + \mathcal{O}\!\left(\frac{J^2}{\Delta_{\rm AB}}\right). \end{aligned} \tag{B9}$$

At leading order, these are the dispersion relations of two independent triangular lattices associated with the A and B sublattices, respectively.

Appendix C: Obtaining the Bose–Hubbard parameters

In this Appendix, we summarize the numerical procedure used to extract the parameters of the tight-binding models. The tunneling parameters and sublattice offset are obtained by fitting tight binding models to the continuous-space single-particle band dispersion relation. The onsite interaction energies are then computed as contact-interaction matrix elements using the corresponding Wannier functions.

1. Fitting the tunneling parameters

For each value of V_0 and ϕ_g, we diagonalize the continuous-space single-particle Hamiltonian $\hat{H}_0$ on a uniform grid of quasimomenta in the first Brillouin zone. The tight-binding dispersions introduced in Appendix B are then fitted to the resulting two lowest subbands.

For the nearest-neighbor and triangular models, the number of fitting parameters is small and the fit is performed directly by standard least-squares minimization. For the full next-nearest-neighbor model, the four parameters J, J'_{A}, J'_{B}, Δ_{AB}, can differ by several orders of magnitude, especially in the regime where the two sublattices progressively decouple. In this case, we first use a differential-evolution algorithm to generate robust initial guesses. These values are then used as starting points for a standard least-squares fit. At the level of the differential-evolution procedure, we include a smoothness penalty to avoid spurious jumps of the fitted parameters between neighboring values of ϕ_g.

2. Obtaining interaction energies

The onsite interaction energies, U_{A} and U_{B} of the BHm of Eq. (6), are computed from maximally localized Wannier functions associated with the lowest band manifold, which contains two subbands corresponding to the two sites of the unit cell. Starting from the Bloch eigenstates obtained by exact diagonalization of $\hat{H}_0$, we construct the input matrices required by Wannier90 [60]: the Bloch eigenvalues, the overlap matrices between neighboring quasimomenta, and the projections onto localized trial orbitals centered on the A and B sites.

The Wannierization procedure yields localized orbitals $w_{\mathrm{A}}(\mathbf{r}-\mathbf{R}_j)$ and $w_{\mathrm{B}}(\mathbf{r}-\mathbf{R}_j)$. For contact interactions, the corresponding onsite interaction energies are then computed as

$$U_{\mathrm{A/B}} = \tilde{g} \int d\mathbf{r}\, |w_{\mathrm{A/B}}(\mathbf{r})|^4 \,, \tag{C1}$$

with $\tilde{g}$ given by Eq. (4). The integrals are evaluated numerically on the real-space grid used for the continuous-space calculations.

Appendix D: Density-assisted tunneling

In the main text, we argued that density-assisted tunneling provides a significant correction to the nearest-neighbor hopping in the honeycomb lattice, even for $V_0 = 15\, E_r$. Here we quantify this effect using the Wannier functions obtained as described in Appendix C.

The density-assisted tunneling amplitude is evaluated as

$$\tilde{J}\,(\tilde{g}) = -\tilde{g} \int d\mathbf{r}\, |w_{\mathrm{A}}(\mathbf{r})|^2 w^*_{\mathrm{A}}(\mathbf{r}) w_{\mathrm{B}}(\mathbf{r}). \tag{D1}$$

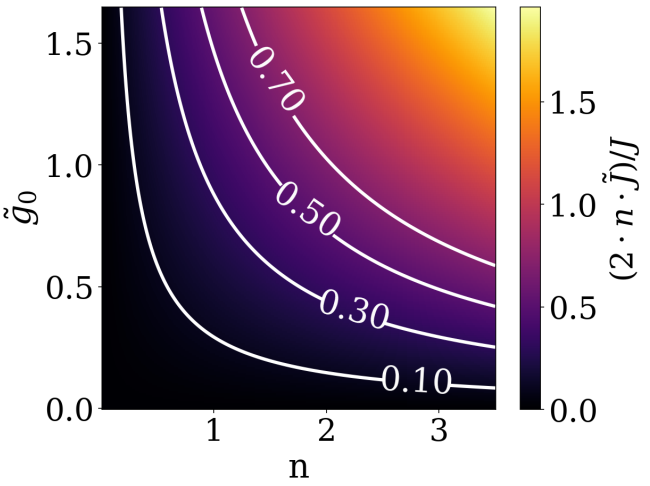

Figure 8. Mean-field estimate of the relative density-assisted tunneling correction, $2n\tilde{J}/J$, as a function of density n and bare coupling $\tilde{g}_0$ for $V_0 = 15\, E_r$. Contours indicate corrections of 10%, 30%, 50%, and 70% relative to the bare nearest-neighbor hopping.

To simplify the discussion and avoid computing the density versus chemical potential over a wide range, we use below $\tilde{J}_0 = \tilde{J}\,(\tilde{g}_0)$. Since the renormalized coupling $\tilde{g}$ is generally larger than $\tilde{g}_0$ in the parameter range considered, this gives a conservative estimate of the DAT contribution.

Within the mean-field estimate used in the main text, the DAT term renormalizes the hopping according to

$$J_{\mathrm{eff}} = J + 2n\tilde{J}. \tag{D2}$$

The relevant dimensionless quantity for the importance of DAT corrections is the relative contribution $2n\tilde{J}_0/J$, plotted in Fig. 8 as a function of the density n and interaction strength $\tilde{g}_0$, with contour lines in white.

In Fig. 8 we show that the relative contribution is small only at low density and weak interaction. In the region corresponding to the first Mott lobe, $MI_{1,1}$ in Fig. 5(a), it remains modest: at the tip of the lobe it is $\sim 8.5\%$, increasing to 34.1% at $\tilde{g}_0 = 1$. For the second lobe $MI_{2,2}$, it becomes significantly larger, reaching $\sim 30.7\%$ at the tip and 68.2% at $\tilde{g}_0 = 1$. For the third lobe (as predicted by the BHm), the relative contribution is already substantial, with values of $\sim 44.0\%$ at the predicted tip and 102.3% at $\tilde{g}_0 = 1$. For reference, the corrections at the tips of the first and second lobes predicted by the BHm are $\sim 6.8\%$ and 21.1%, respectively.

This behavior explains why the standard nearest-neighbor Bose–Hubbard model remains approximately valid for the first Mott lobe but fails progressively at higher filling.

[1] C. Kittel, *Introduction to Solid State Physics*, 8th ed. (Wiley, 2004).

[2] C. Janot, *Quasicrystals: A Primer*, 2nd ed. (Oxford University Press, 1994).

[3] A. H. Castro Neto, F. Guinea, N. M. R. Peres, K. S. Novoselov, and A. K. Geim, The electronic properties of graphene, Rev. Mod. Phys. **81**, 109 (2009).

[4] R. Bistritzer and A. H. MacDonald, Moiré bands in twisted double-layer graphene, Proc. Nat. Acad. Sci. **108**, 12233 (2011).

[5] E. Y. Andrei, D. K. Efetov, P. Jarillo-Herrero, A. H. MacDonald, K. F. Mak, T. Senthil, E. Tutuc, A. Yazdani, and A. F. Young, The marvels of moiré materials, Nat. Rev. Mater. **6**, 201 (2021).

[6] F. D. M. Haldane, Model for a Quantum Hall effect without Landau levels: Condensed-matter realization of the "parity anomaly", Phys. Rev. Lett. **61**, 2015 (1988).

[7] M. Z. Hasan and C. L. Kane, Colloquium: Topological insulators, Rev. Mod. Phys. **82**, 3045 (2010).

[8] K. Kamiya, T. Takeuchi, N. Kabeya, N. Wada, T. Ishimasa, A. Ochiai, K. Deguchi, K. Imura, and N. Sato, Discovery of superconductivity in quasicrystal, Nat. Comm. **9**, 1 (2018).

[9] A. Uri, S. C. de la Barrera, M. T. Randeria, D. Rodan-Legrain, T. Devakul, P. J. D. Crowley, N. Paul, K. Watanabe, T. Taniguchi, R. Lifshitz, L. Fu, R. C. Ashoori, and P. Jarillo-Herrero, Superconductivity and strong interactions in a tunable moiré quasicrystal, Nature (London) **620**, 762 (2023).

[10] S. Rolof, S. Thiem, and M. Schreiber, Electronic wave functions of quasiperiodic systems in momentum space, Eur. Phys. J. B **86**, 372 (2013).

[11] F. Evers and A. D. Mirlin, Anderson transitions, Rev. Mod. Phys. **80**, 1355 (2008).

[12] H. Huang and F. Liu, Quantum spin Hall effect and spin Bott index in a quasicrystal lattice, Phys. Rev. Lett. **121**, 126401 (2018).

[13] M. Lewenstein, A. Sanpera, V. Ahufinger, B. Damski, A. Sen, and U. Sen, Ultracold atomic gases in optical lattices: Mimicking condensed matter physics and beyond, Adv. Phys. **56**, 243 (2007).

[14] I. Bloch, J. Dalibard, and W. Zwerger, Many-body physics with ultracold gases, Rev. Mod. Phys. **80**, 885 (2008).

[15] I. Bloch, J. Dalibard, and S. Nascimbène, Quantum simulations with ultracold quantum gases, Nat. Phys. **8**, 267 (2012).

[16] C. Gross and I. Bloch, Quantum simulations with ultracold atoms in optical lattices, Science **357**, 995 (2017).

[17] T. Esslinger, Fermi-Hubbard physics with atoms in an optical lattice, Annual Rev. Cond. Mat. Phys. **1**, 129 (2010).

[18] L. Tarruell and L. Sanchez-Palencia, Quantum simulation of the Hubbard model with ultracold fermions in optical lattices, C. R. Phys. **19**, 365 (2018); L. Sanchez-Palencia, Quantum simulation: From basic principles to applications, *ibid.* **19**, 357 (2018).

[19] G. Modugno, Anderson localization in Bose-Einstein condensates, Rep. Prog. Phys. **73**, 102401 (2010).

[20] L. Sanchez-Palencia and M. Lewenstein, Disordered quantum gases under control, Nat. Phys. **6**, 87 (2010).

[21] D. Jaksch, C. Bruder, J. I. Cirac, C. W. Gardiner, and P. Zoller, Cold bosonic atoms in optical lattices, Phys. Rev. Lett. **81**, 3108 (1998).

[22] P. Windpassinger and K. Sengstock, Engineering novel optical lattices, Rep. Prog. Phys. **76**, 086401 (2013).

[23] G. Wirth, M. Ölschläger, and A. Hemmerich, Evidence for orbital superfluidity in the p-band of a bipartite optical square lattice, Nat. Phys. **7**, 147 (2011).

[24] C. Becker, P. Soltan-Panahi, J. Kronjäger, S. Dörscher, K. Bongs, and K. Sengstock, Ultracold quantum gases in triangular optical lattices, New J. Phys. **12**, 065025 (2010).

[25] J. Struck, C. Ölschläger, R. Le Targat, P. Soltan-Panahi, A. Eckardt, M. Lewenstein, P. Windpassinger, and K. Sengstock, Quantum simulation of frustrated classical magnetism in triangular optical lattices, Science **333**, 996 (2011).

[26] L. Tarruell, D. Greif, T. Uehlinger, G. Jotzu, and T. Esslinger, Creating, moving and merging Dirac points with a Fermi gas in a tunable honeycomb lattice, Nature (London) **483**, 302 (2012).

[27] N. Fläschner, B. Rem, M. Tarnowski, D. Vogel, D.-S. Lühmann, K. Sengstock, and C. Weitenberg, Experimental reconstruction of the Berry curvature in a Floquet Bloch band, Science **352**, 1091 (2016).

[28] S. Taie, H. Ozawa, T. Ichinose, T. Nishio, S. Nakajima, and Y. Takahashi, Coherent driving and freezing of bosonic matter wave in an optical Lieb lattice, Science Advances **1**, e1500854 (2015).

[29] L. Santos, M. A. Baranov, J. I. Cirac, H.-U. Everts, H. Fehrmann, and M. Lewenstein, Atomic quantum gases in Kagomé lattices, Phys. Rev. Lett. **93**, 030601 (2004).

[30] G.-B. Jo, J. Guzman, C. K. Thomas, P. Hosur, A. Vishwanath, and D. M. Stamper-Kurn, Ultracold atoms in a tunable optical kagome lattice, Phys. Rev. Lett. **108**, 045305 (2012).

[31] M. Anderlini, P. J. Lee, B. L. Brown, J. Sebby-Strabley, W. D. Phillips, and J. V. Porto, Controlled exchange interaction between pairs of neutral atoms in an optical lattice, Nature (London) **448**, 452 (2007).

[32] S. Trotzky, P. Cheinet, S. Fölling, M. Feld, U. Schnorrberger, A. M. Rey, A. Polkovnikov, E. A. Demler, M. D. Lukin, and I. Bloch, Time-resolved observation and control of superexchange interactions with ultracold atoms in optical lattices, Science **319**, 295 (2008).

[33] L. Sanchez-Palencia and L. Santos, Bose-Einstein condensates in optical quasicrystal lattices, Phys. Rev. A **72**, 053607 (2005).

[34] A. Jagannathan and M. Duneau, An eightfold optical quasicrystal with cold atoms, Europhys. Lett. **104**, 66003 (2013).

[35] K. Viebahn, M. Sbroscia, E. Carter, J.-C. Yu, and U. Schneider, Matter-wave diffraction from a quasicrystalline optical lattice, Phys. Rev. Lett. **122**, 110404 (2019).

[36] M. N. Kosch, L. Asteria, H. P. Zahn, K. Sengstock, and C. Weitenberg, Multifrequency optical lattice for dynamic lattice-geometry control, Phys. Rev. Research **4**, 043083 (2022).

[37] C. D. Brown, S.-W. Chang, M. N. Schwarz, T.-H. Leung, V. Kozii, A. Avdoshkin, J. E. Moore, and D. M.

Stamper-Kurn, Direct geometric probe of singularities in band structure, Science **377**, 1319 (2022).
[38] T. Shimasaki, Y. Bai, H. E. Kondakci, P. Dotti, J. E. Pagett, A. R. Dardia, M. Prichard, A. Eckardt, and D. M. Weld, Reversible phasonic control of a quantum phase transition in a quasicrystal, Phys. Rev. Lett. **133**, 083405 (2024).
[39] A. O. Neely, C. C. Wilson, R. Everly, Y. Yao, R. F. Zanetti, and C. D. Brown, Programmable dynamic phase control of a quasiperiodic optical lattice, arXiv:2604.07631 (2026).
[40] K. S. Novoselov, A. K. Geim, S. V. Morozov, D.-e. Jiang, Y. Zhang, S. V. Dubonos, I. V. Grigorieva, and A. A. Firsov, Electric field effect in atomically thin carbon films, Science **306**, 666 (2004).
[41] A. K. Geim and K. S. Novoselov, The rise of graphene, Nat. Mater. **6**, 183 (2007).
[42] S. Miao, Z. Zhang, Y. Zhao, Z. Zhao, H. Wang, and J. Hu, Bosonic fractional quantum Hall conductance in shaken honeycomb optical lattices without flat bands, Phys. Rev. B **106**, 054310 (2022).
[43] M. Hirata, A. Kobayashi, C. Berthier, and K. Kanoda, Interacting chiral electrons at the 2D Dirac points: A review, Rep. Prog. Phys. **84**, 036502 (2021).
[44] P. Soltan-Panahi, D.-S. Lühmann, J. Struck, P. Windpassinger, and K. Sengstock, Quantum phase transition to unconventional multi-orbital superfluidity in optical lattices, Nat. Phys. **8**, 71 (2012).
[45] P. Soltan-Panahi, J. Struck, P. Hauke, A. Bick, W. Plenkers, G. Meineke, C. Becker, P. Windpassinger, M. Lewenstein, and K. Sengstock, Multi-component quantum gases in spin-dependent hexagonal lattices, Nat. Phys. **7**, 434 (2011).
[46] P. St-Jean, A. Dauphin, P. Massignan, B. Real, O. Jamadi, M. Milićević, A. Lemaître, A. Harouri, L. Le Gratiet, I. Sagnes, S. Ravets, J. Bloch, and A. Amo, Measuring topological invariants in a polaritonic analog of graphene, Phys. Rev. Lett. **126**, 127403 (2021).
[47] B. Real, O. Jamadi, M. Milićević, A. Lemaître, L. Le Gratiet, A. Harouri, I. Sagnes, J. Bloch, and A. Amo, Semi-Dirac transport and anisotropic localization in polariton honeycomb lattices, Phys. Rev. Lett. **125**, 186601 (2020).
[48] P. R. Wallace, The band theory of graphite, Phys. Rev. **71**, 622 (1947).
[49] E. Anisimovas, F. Gerbier, T. Andrijauskas, and N. Goldman, Design of laser-coupled honeycomb optical lattices supporting Chern insulators, Phys. Rev. A **89**, 013632 (2014).
[50] J. Kusk Block and N. Nygaard, Honeycomb optical lattices with harmonic confinement, Phys. Rev. A **81**, 053421 (2010).
[51] N. Teichmann, D. Hinrichs, and M. Holthaus, Reference data for phase diagrams of triangular and hexagonal bosonic lattices, Europhys. Lett. **91**, 10004 (2010).
[52] Z. Lin, J. Zhang, and Y. Jiang, Quantum phase transitions of ultracold Bose systems in nonrectangular optical lattices, Phys. Rev. A **85**, 023619 (2012).
[53] W.-W. Wang, J. Yang, J.-P. Lv, and C. Zhang, Bose–Hubbard model on a honeycomb superlattice: Quantum phase transitions and lattice effects, Phys. Rev. A **112**, 043320 (2025).
[54] D. S. Petrov, M. Holzmann, and G. V. Shlyapnikov, Bose–Einstein condensation in quasi-2D trapped gases, Phys. Rev. Lett. **84**, 2551 (2000).
[55] D. Petrov and G. Shlyapnikov, Interatomic collisions in a tightly confined Bose gas, Phys. Rev. A **64**, 012706 (2001).
[56] L. Pricoupenko and M. Olshanii, Stability of two-dimensional Bose gases in the resonant regime, J. Phys. B: At. Mol. Opt. Phys. **40**, 2065 (2007).
[57] R. Gautier, H. Yao, and L. Sanchez-Palencia, Strongly interacting bosons in a two-dimensional quasicrystal lattice, Phys. Rev. Lett. **126**, 110401 (2021).
[58] S. Javvaji, F. Li, and J. Jung, Ab initio tight-binding models for mono- and bilayer hexagonal boron nitride (h-BN), Phys. Rev. Mater. **9**, 024004 (2025).
[59] K. Kishigi, R. Takeda, and Y. Hasegawa, Energy gap of tight-binding electrons on generalized honeycomb lattice, J. Phys. Conf. Ser. **132**, 012005 (2008).
[60] G. Pizzi, V. Vitale, R. Arita, S. Blügel, F. Freimuth, G. Géranton, M. Gibertini, D. Gresch, C. Johnson, T. Koretsune, J. Ibañez-Azpiroz, H. Lee, J.-M. Lihm, D. Marchand, A. Marrazzo, Y. Mokrousov, J. I. Mustafa, Y. Nohara, Y. Nomura, L. Paulatto, S. Poncé, T. Ponweiser, J. Qiao, F. Thöle, S. S. Tsirkin, M. Wierzbowska, N. Marzari, D. Vanderbilt, I. Souza, A. A. Mostofi, and J. R. Yates, Wannier90 as a community code: New features and applications, J. Phys.: Cond. Matt. **32**, 165902 (2020).
[61] C. L. Fefferman and M. I. Weinstein, Honeycomb lattice potentials and Dirac points, J. Am. Math. Soc. **25**, 1169 (2012).
[62] C. Wu and S. Das Sarma, $p_{x,y}$-orbital counterpart of graphene: Cold atoms in the honeycomb optical lattice, Phys. Rev. B **77**, 235107 (2008).
[63] M. Boninsegni, N. Prokof'ev, and B. Svistunov, Worm algorithm for continuous-space path integral Monte Carlo simulations, Phys. Rev. Lett. **96**, 070601 (2006).
[64] D. M. Ceperley, Path integrals in the theory of condensed helium, Rev. Mod. Phys. **67**, 279 (1995).
[65] V. L. Berezinskii, Destruction of long range order in one-dimensional and two-dimensional systems having a continuous symmetry group. 1. classical systems, Sov. Phys. JETP **32**, 493 (1971).
[66] J. M. Kosterlitz and D. J. Thouless, Ordering, metastability and phase transitions in two-dimensional systems, J. Phys. C: Solid State Phys. **6**, 1181 (1973).
[67] D. R. Nelson and J. M. Kosterlitz, Universal jump in the superfluid density of two-dimensional superfluids, Phys. Rev. Lett. **39**, 1201 (1977).
[68] M. Ciardi, T. Macrì, and F. Cinti, Finite-temperature phases of trapped bosons in a two-dimensional quasiperiodic potential, Phys. Rev. A **105**, L011301 (2022).
[69] Z. Zhu, H. Yao, and L. Sanchez-Palencia, Thermodynamic phase diagram of two-dimensional bosons in a quasicrystal potential, Phys. Rev. Lett. **130**, 220402 (2023).
[70] D. Johnstone, S. Mishra, Z. Zhu, H. Yao, and L. Sanchez-Palencia, Weak superfluidity in twisted optical potentials, Phys. Rev. Research **6**, L042066 (2024).